Journal of Alloys and Compounds 898 (2022) 162890

Contents lists available at ScienceDirect

Journal of Alloys and Compounds

journal homepage: www.elsevier.com/locate/jalcom

Strain hardening behavior of additively manufactured and annealed AlSi3.5Mg2.5 alloy

X.X. Zhang[a,*,1], A. Lutz[b], H. Andrä[a], M. Lahres[b], W. Gong[c], S. Harjo[d], C. Emmelmann[e]

[a] Fraunhofer Institute for Industrial Mathematics ITWM, Fraunhofer-Platz 1, 67663 Kaiserslautern, Germany
[b] Mercedes Benz AG, Research and Development Department, Leibnizstraße 2, 71032 Böblingen, Germany
[c] Elements Strategy Initiative for Structural Materials, Kyoto University, Yoshida-honmachi, Sakyo-ku, Kyoto 606-8501, Japan
[d] J-PARC Center, Japan Atomic Energy Agency, 2-4 Shirane Shirakata, Tokai, Naka, Ibaraki 319-1195, Japan
[e] Institute of Laser and System Technologies, Hamburg University of Technology (TUHH), Denickestraße 17, D-21073 Hamburg, Germany

ARTICLE INFO

Article history:
Received 11 October 2021
Accepted 19 November 2021
Available online 25 November 2021

Keywords:
Aluminum alloy
Additive manufacturing
Laser powder bed fusion (LPBF)
Neutron diffraction
Strain hardening behavior
Dislocation density
Kocks-Mecking model

ABSTRACT

The ductility of the Al alloys produced by additive manufacturing (AM) has become a critical property, as the AM Al alloys are increasingly used in the automotive industry. However, the ductility of as-built AM Al alloys is relatively low, even with optimized AM conditions. The post-annealing treatment provides an efficient way to improve ductility. Previous investigation has shown that the annealed AM AlSi3.5Mg2.5 alloy possesses superior ductility. However, the plastic deformation micro-mechanisms of the annealed AM AlSi3.5Mg2.5 alloy remain unclear. In this study, in-situ neutron diffraction was employed to explore the annealed AM AlSi3.5Mg2.5 alloy. The evolutions of phase stresses, dislocation density, and crystallite size in the annealed AM AlSi3.5Mg2.5 alloy during tensile deformation were analyzed. The experimental investigation reveals that the dislocation density in the Al matrix of the annealed AM AlSi3.5Mg2.5 alloy increases slowly in the early plastic deformation stage, and it reaches a saturated level upon the following uniform deformation. The crystallite size decreases quickly in the early deformation stage, and then it decreases slowly. The Kocks-Mecking model and the Voce model can capture the strain hardening behavior well. The determined physical constitutive equations can be applied in continuum mechanical computer simulations.

© 2021 The Author(s). Published by Elsevier B.V.
CC_BY_NC_ND_4.0

1. Introduction

As the Al alloys are increasingly applied in the automotive industry, their ductility has become a critical property. During an automotive crash incident, the folding and bending components are desirable for energy absorption. Hence, high ductility is crucial to guarantee energy adsorption capacity and vehicle safety. Al components produced via additive manufacturing (AM) that have optimized geometry and reduce the usage of fasteners can provide an excellent lightweight benefit to the automotive industry.

However, the as-built AM Al alloys usually show relatively low ductility [1]. On the one hand, the low ductility is partially associated with defects like the non-negligible porosity, which can be minimized through optimizing the AM conditions [2,3]. On the other hand, the ductility decreases when the strength is high due to a strength-ductility trade-off. Hence, the AM conditions should be optimized to obtain high ductility. Furthermore, a post-heat treatment, e.g., annealing treatment, can be employed.

Compared with the well-known AM AlSi10Mg alloy, a novel AM AlSi3.5Mg2.5 alloy free of rare-earth elements possesses better ductility [4,5]. For instance, Lutz et al. [5] reported that the total elongation of the laser powder bed fusion (LPBF) AlSi3.5Mg2.5 after annealing is 26.7 ± 1.3%, about 31% higher than that of the annealed LPBF AlSi10Mg. Knoop et al. [4] showed that the tight bending angle of the annealed LPBF AlSi3.5Mg2.5 is 96.5 ± 3.0°, almost twice that of the annealed LPBF AlSi10Mg. Additionally, a high strain hardening exponent n = 0.18 is measured for the annealed LPBF AlSi3.5Mg2.5 [5], about twice those of the casting Al-Si-Mg alloys [6,7]. Although previous results have indicated a superior ductility of the annealed LPBF AlSi3.5Mg2.5 alloy [4,5], the uniform elongation (~11.3%) of this annealed LPBF AlSi3.5Mg2.5 alloy is not improved much compared with the total elongation [5], limiting its extensive industrial

* Corresponding author.
E-mail address: xingxing.zhang@frm2.tum.de (X.X. Zhang).
[1] Present address: Heinz Maier-Leibnitz Zentrum (MLZ), Technical University of Munich, Lichtenbergstrasse 1, 85748 Garching, Germany

https://doi.org/10.1016/j.jallcom.2021.162890
0925-8388/© 2021 The Author(s). Published by Elsevier B.V.
CC_BY_NC_ND_4.0

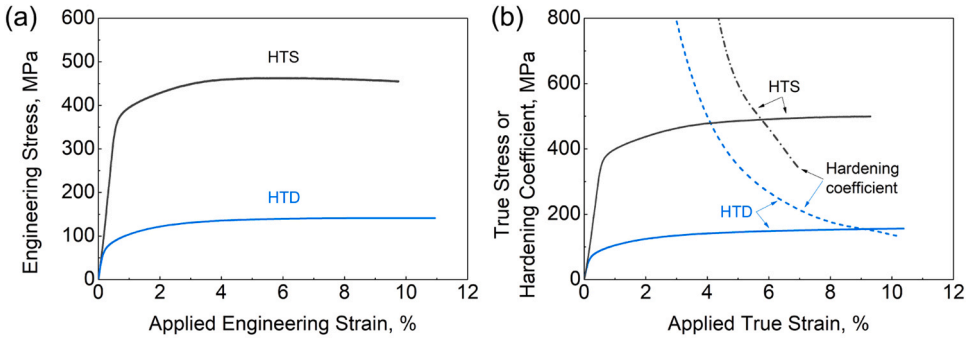

Fig. 1. Macroscopic mechanical properties of HTD and HTS upon the in-situ tests: (a) engineering stress-strain curves; (b) true stress-strain and hardening coefficient curves.

applications. Hence, it is essential to clarify the underlying micro-mechanisms of its plastic deformation to enhance the uniform elongation of the annealed LPBF AlSi3.5Mg2.5 alloy in the future.

Note that the eutectic cell boundaries dissolve after heat treatment at elevated temperatures, and larger Mg_2Si and Si particles form in the AM Al-Si-Mg alloys [5,8,9]. Such a microstructure variation alters the strain hardening behavior and the dislocation activities [10]. For example, the aging treatment disintegrates the cellular-dendrite pattern and promotes precipitation of Mg_2Si and Si, increasing strength. The isolated Mg_2Si and Si particles have weaker constraints to the dislocation motions than the cell boundary network [10].

When the LPBF AlSi3.5Mg2.5 is annealed at 380 °C for one hour, the isolated Mg_2Si and Si particles have even larger sizes and thereby weaker interactions with dislocations [5]. Meanwhile, the annealing treatment causes static recovery, reducing the dislocation density and, in turn, the strength significantly. Then one question arises: How do the dislocations behave in this annealed microstructure during plastic deformation? This study explores the plastic deformation micro-mechanisms of the annealed LPBF AlSi3.5Mg2.5 alloy to reveal the relationship between the dislocation density and the strain hardening behavior.

The annealed LPBF AlSi3.5Mg2.5 alloy was subjected to an in-situ neutron diffraction experiment. The direct-aged LPBF AlSi3.5Mg2.5 alloy was also investigated for comparison. The dislocation density in the Al matrix was analyzed via the convolutional multiple whole profile (CMWP) approach [11,12]. The phase stresses of Al, Mg_2Si, and Si were separated. The strain hardening behavior of the Al matrix was qualified by the Kocks-Mecking model [13] and the Voce model [13,14]. The present investigation provides valuable insights into the ductility of the annealed LPBF AlSi3.5Mg2.5 alloy. Meanwhile, the determined physical constitutive equations can be applied for continuum mechanical computer simulations (i.e., finite element analysis of printed components), capable of predicting the novel alloy's mechanical behavior under various loading conditions.

2. Experimental procedure and methodology

2.1. Material and LPBF process

The AlSi3.5Mg2.5 specimens were manufactured vertically using a Concept Laser M2 UP1 cusing laser system (400 W). The LPBF parameters can be found in the previous investigation [10]. The as-built cylindrical specimens have a diameter of 14 mm and a length of 104 mm. The specimens (namely HTD) were subjected to an annealing treatment at 380 °C for one hour after LPBF in a circulation air oven followed by cooling down at ambient air. For comparison, the direct-aged specimens (namely HTS) were also investigated. The aging treatment was conducted at 170 °C for one hour after LPBF. The heat-treated specimens were then machined to remove rough surfaces, resulting in the dog-bone-shaped specimens with a total length of 76 mm. The gauge part of the dog-bone-shaped specimens has a diameter of 6 mm and a gauge length of 30 mm [15].

The direct-aged specimens were employed for comparison. The previous investigation showed that the initial dislocation density is almost the same in HTS and as-built alloy [10]. The residual stresses in HTS are partially released due to the stress relaxation effect upon the heat treatment [10]. This should also be the case in the HTD sample due to a higher treatment temperature. Accordingly, the effect of residual stress is reduced in both HTD and HTS. Besides, the microstructure of HTD is closer to that of HTS. In contrast, the as-built Al-Si-Mg alloys possess a cellular-dendritic microstructure, causing complex dislocation activities upon plastic deformation that have been reported in our previous investigations [15–17].

2.2. Microstructure characterization, ex-situ tensile tests, and fractography observation

The electron backscatter diffraction (EBSD) samples were prepared via ion milling using a Hitachi ArBlade IM5000 system. The EBSD microstructure was analyzed using the electron microscope Zeiss Auriga with EBSD detector Symmetry (Oxford Instruments). The increment was set to 0.5 μm [10].

Three HTD specimens were subjected to ex-situ tensile tests at a nominal strain rate of 1.0×10^{-3} s^{-1}. For multiphase materials, the elastoplastic deformation at the microscale is inhomogeneous. The localized deformation initiates damage and causes a fracture when the applied strain is large enough. This study used a scanning electron microscope (SEM) to analyze the fractured tensile specimens. The fractured specimen was then analyzed for fractography characterization. A Zeiss LEO 1450VP system was used with an acceleration voltage of 15 kV. The imaging view is parallel to the LD during the tensile test and to the building direction during manufacturing (normal to the base plane of the building platform).

2.3. In-situ neutron diffraction experiments

The in-situ neutron diffraction experiment was conducted at the TAKUMI engineering neutron diffractometer of the Japan Proton Accelerator Research Complex (J-PARC) [18]. The specimens were subjected to monotonic tensile tests at room temperature with a nominal strain rate of 1.1×10^{-5} s^{-1}. This strain rate is slower than that of the ex-situ tensile tests to guaranty a sufficient acquisition time of neutron diffraction pattern. The applied strain was recorded

Table 1
Mechanical properties of the HTD and HTS specimens.

Material	$\dot{\varepsilon}$, s^{-1}	σ_y, MPa	σ_{uts}, MPa	EL, %	Reference
HTD	1.1×10^{-5} for in-situ	77.3	141.1	–	This work
	1.0×10^{-3} for ex-situ	106.0 ± 2.6	184.0 ± 1.4	29.0 ± 1.9	This work
HTS	1.1×10^{-5} for in-situ	381.7	462.5	9.1	This work
	1.0×10^{-3} for ex-situ	417.1 ± 2.8	505.3 ± 3.5	11.0 ± 0.4	[10]

Footnote: $\dot{\varepsilon}$ is the tensile strain rate, σ_y the 0.2% offset yield strength, σ_{uts} the tensile strength, and EL the max plastic strain measured from the strain-stress curve.

using an Epsilon extensometer. The incident beam had a size of $5 \times 6\ mm^2$, and the radial collimators had a width of 5 mm.

The neutron diffraction spectrums were analyzed using the MAUD software to obtain the quantitative contents of all phases [19]. The lattice parameter of each phase was determined using Z-Rietveld software [20] based on the Rietveld refinement method. The average lattice strain $\bar{\varepsilon}_s^i$ in direction s (s = loading direction (LD) or transversal direction (TD)) of phase i (i = Al, Mg_2Si, or Si) is calculated by

$$\bar{\varepsilon}_s^i = \frac{a_s^i}{a_{s,0}^i} - 1 \tag{1}$$

where a_s^i is the refined lattice parameter and $a_{s,0}^i$ the corresponding reference lattice parameter. The LD phase stress $\bar{\sigma}_{LD}^i$ is approximately calculated by

$$\bar{\sigma}_{LD}^i = E_{bulk}^i \bar{\varepsilon}_{LD}^i \tag{2}$$

where E_{bulk}^i is the Young's modulus of phase i.

The CMWP approach was applied to determine the dislocation density and crystallite size of the Al matrix. This CMWP approach developed by Ribarik and Ungar [11,12] has been successfully applied to determine the dislocation densities in various alloys, such as Al alloys [12,21], bainitic steels [22,23], and zirconium hydride [24].

3. Results

3.1. Macroscopic mechanical properties

Fig. 1(a) shows the engineering stress-strain curves of HTD and HTS under in-situ tensile loading. HTD was loaded until 10.4% strain, while the following necking stage was not investigated due to local deformation. HTS was loaded until fracture. The true stress-strain curves (σ_t versus ε_t) and hardening coefficients ($\Theta = d\sigma_t/d\varepsilon_t$) are shown in Fig. 1(b). According to the Considère necking condition $\Theta = \sigma_t$ [25], the determined uniform strain ε_N of HTD and HTS is 9.1% and 5.8%, respectively. The in-situ measured yield and tensile strengths of HTD are 77.3 and 141.1 MPa, respectively. These properties of HTS are 381.7 and 462.5 MPa, respectively. The mechanical properties of HTD and HTS at different tensile strain rates are summarized in Table 1.

3.2. Microstructure and phase compositions

Figs. 2(a) and (b) show the EBSD microstructures in the vertical and horizontal sections, respectively. In the vertical section, columnar grains dominate the grain structure, which is typical in AM alloys. From Fig. 2(a), the grain size was analyzed using the equivalent circle diameter. Statistics indicate that the average grain size in the vertical section is 3.8 ± 0.7 µm. Note that the grains at the EBSD image borders were excluded during statistics. The average grain size in the horizontal section is 3.4 ± 0.6 µm. These grain sizes are slightly larger than those of the as-built and direct-aged (HTS) samples [10], indicating slight grain growth in the HTD sample during the annealing treatment. Besides, the pole figures in Figs. 2(a) and (b) show a characteristic < 001 > //Z fiber texture, as expected [10].

Based on the Rietveld refinement analysis of the neutron diffraction spectrums, the determined volume fractions of the Al, Mg_2Si, and Si phases in HTD are 93.07 ± 0.26%, 4.89 ± 0.24%, and 2.04 ± 0.03%, respectively. The corresponding values in HTS are 94.82 ± 0.34%, 3.65 ± 0.24%, and 1.53 ± 0.10%, respectively. Considering different measuring methods and different specimens, the measured phase contents of HTS in this investigation agree with the previous in-situ synchrotron X-ray diffraction experiment [10]. The volume fractions of Al, Mg_2Si, and Si in the as-built AlSi3.5Mg2.5 alloy are 95.37%, 3.06%, and 1.56%, respectively [10]. Therefore, additional Mg_2Si and Si precipitate out in HTD upon the annealing treatment.

3.3. Lattice strains and phase stresses

The average lattice strains of the Al, Mg_2Si and Si phases in HTD and HTS are shown in Figs. 3(a) and (b), respectively. In the macroscopic elastic stage, all lattice strains are proportional to the applied true stress approximately. Significant errors of the Si lattice strains in HTS exist because of the low Si content and the fine Si particle size (Fig. 3(b)). In the macroscopic plastic stage, the magnitudes of the Al lattice strains increase slowly due to plastic deformation. In contrast, the lattice strains of Mg_2Si and Si in the LD increase rapidly in the macroscopic plastic stage. Moreover, the Mg_2Si and Si lattice strains of HTS in the LD decrease from the applied true stress of 472.9 MPa, indicating a damaging stage. This phenomenon has also been detected in the previous investigation [10].

The phase stresses in HTD are shown in Fig. 3(c). The average stresses in the Mg_2Si and Si phases of HTD are higher than that in the Al phase during plastic deformation. The maximum stresses in the Mg_2Si and Si phases of HTD are about 764 and 814 MPa, respectively. The average phase stresses in HTS are shown in Fig. 3(d). The measured maximum average stresses of Si and Mg_2Si in HTS are about 2305 and 1690 MPa, respectively.

3.4. Dislocation density and strain hardening behavior

The initial total dislocation density in HTD is about $1.40 \times 10^{14}\ m^{-2}$. The total dislocation density increases slowly in the early plastic deformation stage and reaches a saturation value of $\sim 6.00 \times 10^{14}\ m^{-2}$ at the applied true strains > 3.5% (Fig. 4(a)). In contrast, the dislocation density in HTS increases largely and continuously with the applied true strain during uniform deformation. With the applied true strain increasing from 0% to 5.7%, the total dislocation density in HTS increases significantly from 3.22×10^{14} to $24.67 \times 10^{14}\ m^{-2}$ (Fig. 4(a)). The total dislocation density during plastic deformation in the present HTS is lower than that in the previous investigation [10], which should be associated with different tensile strain rates. In the present investigation, the in-situ

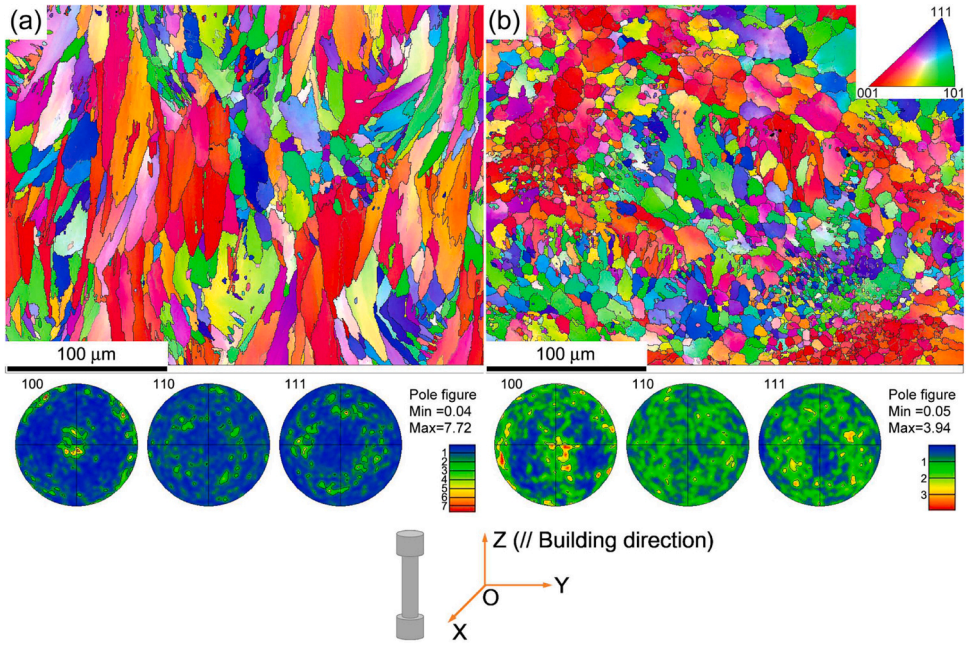

Fig. 2. EBSD microstructure of the LPBF and annealed AlSi3.5Mg2.5 alloy: (a) vertical and (b) horizontal sections.

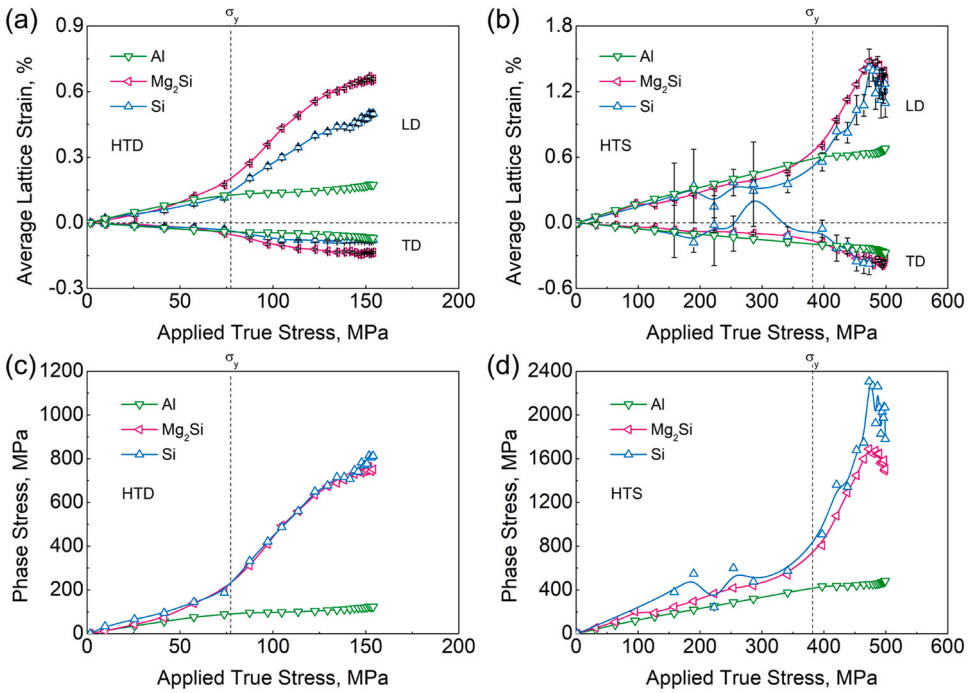

Fig. 3. Microscopic strains and stresses: average lattice strains in (a) HTD and (b) HTS, (d) phase stresses in (c) HTD and (d) HTS. The error bars of average lattice strains of the Al phase are negligible and are therefore not displayed in (a) and (b).

tensile strain rate was 1.1×10^{-5} s^{-1}, whereas it was 1.5×10^{-4} s^{-1} in the previous investigation [10]. The total dislocation density includes mobile and forest dislocation densities. According to the Orowan equation, the strain rate $\dot{\varepsilon}$ relates to the mobile dislocation density ρ_m via [26].

$$\dot{\varepsilon} = Mb\rho_m\bar{v}, \tag{3}$$

where M is the average Taylor factor, b the magnitude of the Burgers vector, and $\bar{v}$ the average dislocation velocity. If the average dislocation velocity is less sensitive to the strain rate $\dot{\varepsilon}$, the mobile dislocation density ρ_m will reduce with decreasing $\dot{\varepsilon}$. This could be one reason that the current total dislocation density in HTS is lower than that in our previous investigation [10].

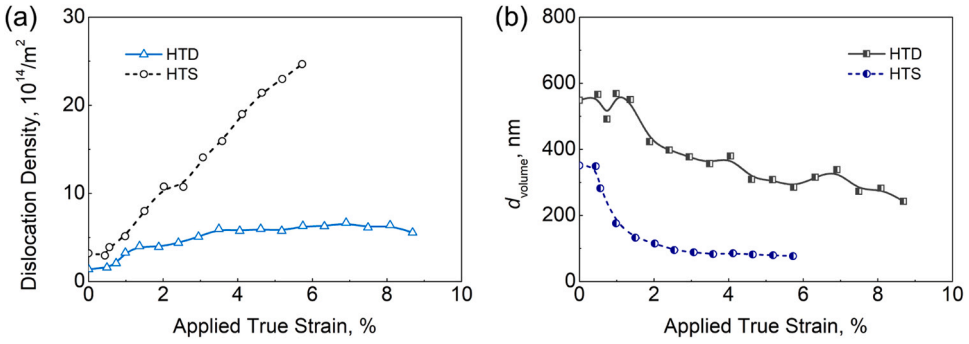

Fig. 4. Evolutions of (a) total dislocation density and (b) volume-weighted mean crystallite size d_{volume} in HTD and HTS.

As the dislocation density increases during plastic deformation, dislocation walls form to reduce the elastic energy [27]. Hence, the crystallite size decreases with increasing the dislocation density [28–30]. Fig. 4(b) shows that the volume-weighted mean crystallite size d_{volume} of HTD decreases from 548 to 243 nm with increasing the applied true strain from 0% to 8.7%, and d_{volume} of HTS decreases from 351 to 77 nm with increasing the applied true strain from 0% to 5.7%.

4. Discussions

4.1. Load transfer mechanism

Fig. 3 reveals that the lattice strains and phase stresses of Mg_2Si and Si are much lower in HTD than in HTS. For multiphase materials consisting of ductile matrix and stiff constituent phases, the phase stresses depend on the geometrical features of the phases (e.g., the size, aspect ratio, and distribution of stiff particles [31–33]), the constitutive behavior [34] of all phases, and the properties of interfaces between phases [35,36]. In this study, the yield strength and the flow stress are much lower in HTD than in HTS. Previous crystal plasticity investigation showed that the stress in the stiff phase is low when the matrix's yield strength and flow stress are low due to a weak load transfer effect [37]. Moreover, the Mg_2Si and Si particles have smaller aspect ratios in HTD (where the particles are nearly spherical [5]) than in HTS (where the particles are less spherical [10]), which also contribute to a weaker load transfer effect in HTD [38].

No apparent damaging effect is detected in the Mg_2Si and Si phases of HTD because the phase stresses are relatively low. In contrast, the lattice strains and phase stresses of Mg_2Si and Si in HTS are very high. An apparent damaging phenomenon is detected in HTS, i.e., the Mg_2Si and Si lattice strains in the LD decrease after the applied true stress of 472.9 MPa.

4.2. Strain hardening mechanism

During strain hardening stage, the relationship between dislocation density ρ and mechanical stress σ can be evaluated by the Taylor equation [39].

$$\sigma = \sigma_0 + M\alpha\mu b\sqrt{\rho}, \tag{4}$$

where σ_0 is the initial friction stress, the average Taylor factor $M = 3.06$ for face-centered cubic metals with random texture [40,41], α the strengthening coefficient, μ the shear modulus (μ = 26.38 GPa for Al), and b the Burgers vector (b = 0.286 nm for Al).

In this investigation, large measurement errors exist in the LD and TD strains of the Si phase. Moreover, the Si TD strain at the applied true strains > 3.6% cannot be determined. Therefore, Eq. (2) was employed to determine the average stresses in all phases approximately. Figs. 5(a) and (b) show the Al phase stress versus $\sqrt{\rho}$ relation for HTD and HTS, respectively. Both of them can be predicted by the Taylor equation. The determined values of the strengthening coefficient α for the Al phase in HTD and HTS are 0.10 and 0.046, respectively. The latter one agrees with the previous value ($\alpha = 0.047$ for the Al phase in HTS) determined from in-situ synchrotron X-ray diffraction [10].

Furthermore, the strain hardening behavior can be described by the Kocks-Mecking (K-M) model [13,42], which qualifies the relation between dislocation density and plastic strain. The original K-M model reads [13].

$$\frac{d\rho}{d\varepsilon_p} = k_1\sqrt{\rho} - k_2\rho, \tag{5}$$

where the parameter k_1 is associated with the thermal storage of mobile dislocations, and the parameter k_2 accounts for the dislocation annihilation due to dynamic recovery. With constant parameters k_1 and k_2 at a certain microstructure, Eq. (5) can be integrated into [10].

$$\varepsilon_p = k_0 - \frac{2}{k_2}\ln|k_1 - k_2\sqrt{\rho}|, \tag{6}$$

where $k_0 = (2\ln|k_1 - k_2\sqrt{\rho_0}|)/k_2$, and ρ_0 is the initial dislocation density.

Figs. 5(c) and (d) show the evolutions of Al plastic strain with $\sqrt{\rho}$ for HTD and HTS, which are well captured by a monotonous K-M model. It can be seen that the k_1 value of HTD is only ~54% of the HTS one, while the k_2 value of HTD is ~128% of the HTS one. Compared with HTS, a much smaller k_1 value in HTD indicates a much lower dislocation storage rate in HTD, while a higher k_2 value in HTD reveals a higher dislocation annihilation rate in HTD. The differences in the k_1 and k_2 parameters between HTD and HTS should be associated with the microstructure. Firstly, a static recovery process occurs during the annealing process, reducing the total dislocation density in HTD. The dislocation densities in Fig. 4(a) show that the initial dislocation density in HTD is only about 43% of that in HTS. Secondly, the Mg_2Si and Si particles are larger and more spherical in HTD, decreasing the stress concentrations during plastic deformation. Thirdly, the crystallite size is larger in HTD than in HTS (Fig. 4(b)). These results reveal that the densities of dislocation sources and obstacles in HTD are lower than those in HTS. Accordingly, HTD exhibits a lower dislocation-storage rate and a higher dislocation-annihilation rate than HTS.

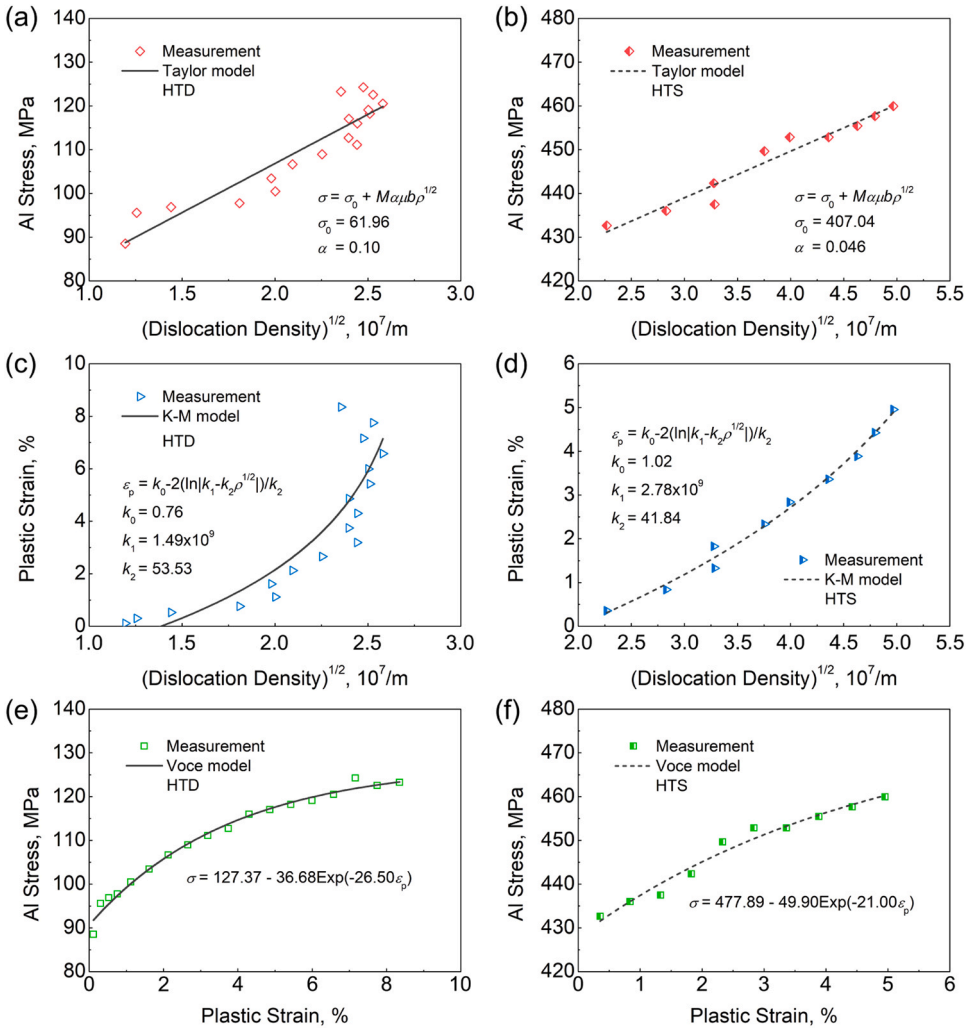

Fig. 5. Relationships between the dislocation density, Al phase stress, and plastic strain for (left) HTD and (right) HTS: (a) and (b) Al stress versus $\sqrt{\rho}$; (c) and (d) plastic strain versus $\sqrt{\rho}$; (e) and (f) Al stress versus plastic strain.

Following the K-M model, the relationship between mechanical stress σ and plastic strain ε_p can be calculated by the Voce model [13]:

$$\sigma = \sigma_s - (\sigma_s - \sigma_c)\exp(-n_c\varepsilon_p), \tag{7}$$

where σ_c is the initial yield stress, σ_s the saturation stress, and n_c the characteristic factor. Figs. 5(e) and (f) show that the relations between σ and ε_p can be well captured by the Voce model. Theoretically, this k_2/n_c ratio should equal two as justified by the K-M model [13,15]. Here, the determined k_2/n_c values for HTD and HTS are 2.02 and 1.99, respectively. Therefore, the present quantitative analysis of the stain hardening behavior is validated.

4.3. Fracture mechanism

The average lattice strains of the Al, Mg_2Si and Si phases in Fig. 3 indicate heterogeneous deformation at the microscale. After the yield point, the dislocation density in the Al phase increases upon the plastic deformation (Fig. 4). Since the stiff Mg_2Si and Si particles act as obstacles for dislocation motions, dislocations accumulate around the second phase particles [43,44]. Consequently, the stiff Mg_2Si and Si particles serve as void nucleation sites at large plastic deformation [45,46]. Here, the fracture surface of an ex-situ HTD specimen tested at 1.0×10^{-3} s^{-1} strain rate is characterized by SEM. An overview of the cone fracture is shown in Fig. 6(a), and a zoomed view of the center part is shown in Fig. 6(b). The fracture surface of HTD is no longer along the melt pool boundary, different from those of the as-built and HTS states [10,47]. This behavior is associated with the distribution of second phase particles, which are much more homogeneous in HTD than in the as-built alloy [48]. A high-magnification view of the center part shows the equiaxial dimples clearly (Fig. 6(c)). Many dimples contain spherical particles, as indicated by the white arrows in Fig. 6(c). These results suggest that the fracture mode of HTD is a ductile fracture with the mechanism of void nucleation, growth, and coalescence. Moreover, the particles inside dimples confirm that the second phase particles serve as void nucleation sites. A high-magnification view of the marginal area of the cone fracture is shown in Fig. 6(d), where the traces of shear sliding are clear.

The K-M model analysis in Figs. 5(c) and (d) reveals that the dislocation storage rate of HTD is much lower than that of HTS, while the dislocation annihilation rate of HTD is higher than that of HTS. Accordingly, the accumulation of dislocations around the Mg_2Si and

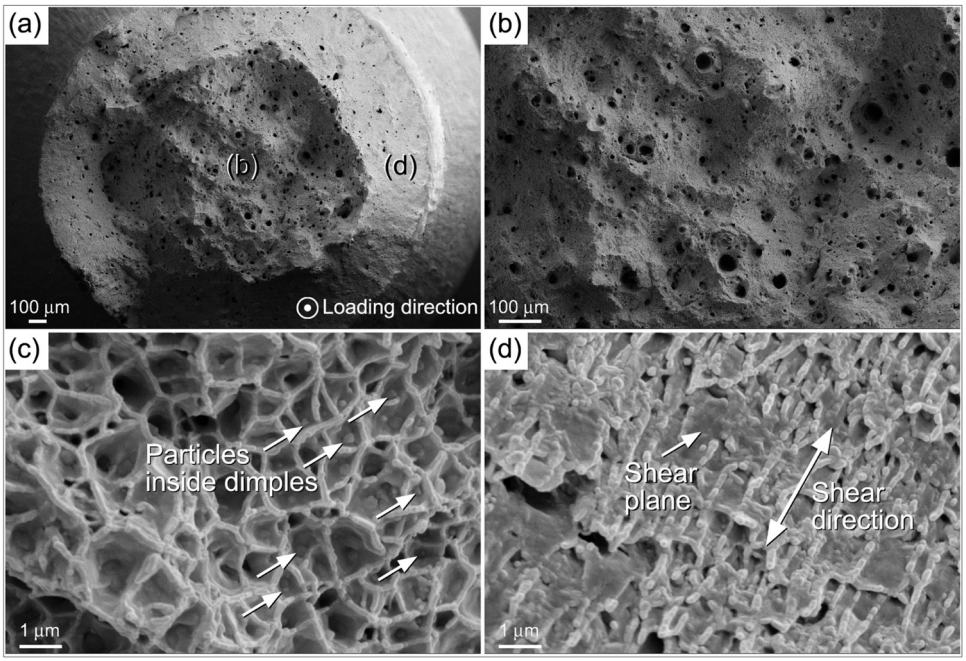

Fig. 6. Fractographs of the ex-situ HTD specimen tested at 1.0×10^{-3} s^{-1} strain rate: (a) an overview of the cone fracture, (b) a zoomed view of the center area, high-magnification views of the (c) center area, and (d) marginal area.

Si particles is more difficult in HTD than in HTS. Therefore, the void nucleation is slower in HTD than in HTS. This mechanism contributes to the higher elongation of HTD compared with HTS.

5. Conclusions

(1) According to the evolutions of lattice strains in the phases, no noticeable damage effects are observed in Mg_2Si and Si of HTD during uniform deformation. The damaging effect is detected in the Mg_2Si and Si phases of HTS, agreeing with the previous investigation [10]. The fracture surfaces of HTD and HTS indicate a ductile fracture mode.

(2) The total dislocation density in HTD increases slowly with the applied true strains < 3.5%, and then it remains almost constant during the following uniform deformation. In contrast, the dislocation density in HTS increases rapidly with the applied strain. The initial crystallite size is larger in HTD than in HTS. For both HTD and HTS, the crystallite sizes decrease quickly in the early deformation stage, and then it decreases slowly.

(3) The dislocation storage rate is much lower in HTD than in HTS, while the dislocation annihilation rate is higher in HTD than in HTS. As a result, the dislocation accumulation around the Mg_2Si and Si particles is more difficult in HTD than in HTS, contributing to a higher ductility in HTD. The identified K-M and Voce models can be used in advanced crystal plasticity models for predicting the printed components' mechanical behavior under various loading conditions, as demonstrated in the references [49–51].

Declaration of Competing Interest

The authors declare that they have no known competing financial interests or personal relationships that could have appeared to influence the work reported in this paper.

Acknowledgments

The authors gratefully acknowledge support from the project CustoMat_3D, which was sponsored by the German Federal Ministry of Education and Research (BMBF) with No. 03XP0101I. This work was also supported by the Fraunhofer Cluster of Excellence "Programmable Materials" (CPM). The neutron diffraction experiments were performed at TAKUMI in the Materials and Life Science Experimental Facility of J-PARC with the proposal of 2019B0075. The authors are grateful to the beamline team of TAKUMI at J-PARC, Japan, for their kind support of the experiments.

References

[1] B. Chen, S.K. Moon, X. Yao, G. Bi, J. Shen, J. Umeda, K. Kondoh, Strength and strain hardening of a selective laser melted AlSi10Mg alloy, Scr. Mater. 141 (2017) 45–49.
[2] J. Samei, M. Amirmaleki, M.S. Dastgiri, C. Marinelli, D.E. Green, In-situ X-ray tomography analysis of the evolution of pores during deformation of AlSi10Mg fabricated by selective laser melting, Mater. Lett. 255 (2019) 126512.
[3] N.T. Aboulkhair, N.M. Everitt, I. Ashcroft, C. Tuck, Reducing porosity in AlSi10Mg parts processed by selective laser melting, Addit. Manuf. 1–4 (2014) 77–86.
[4] D. Knoop, A. Lutz, B. Mais, A. von Hehl, A tailored AlSiMg alloy for laser powder bed fusion, Metals 10 (2020) 514.
[5] A. Lutz, L. Huber, C. Emmelmann, Strain rate dependent material properties of selective laser melted AlSi10Mg and AlSi3.5Mg2.5, Mater. Test. 62 (2020) 573–583.
[6] C.H. Caceres, B.I. Selling, Casting defects and the tensile properties of an Al-Si-Mg alloy, Mater. Sci. Eng. A 220 (1996) 109–116.
[7] J.G. Kaufman, E.L. Rooy, Aluminum Alloy Castings: Properties, Processes And Applications, ASM International, 2004.
[8] K.G. Prashanth, S. Scudino, H.J. Klauss, K.B. Surreddi, L. Lober, Z. Wang, A.K. Chaubey, U. Kuhn, J. Eckert, Microstructure and mechanical properties of Al-12Si produced by selective laser melting: effect of heat treatment, Mater. Sci. Eng. A 590 (2014) 153–160.
[9] W. Li, S. Li, J. Liu, A. Zhang, Y. Zhou, Q.S. Wei, C.Z. Yan, Y.S. Shi, Effect of heat treatment on AlSi10Mg alloy fabricated by selective laser melting: microstructure evolution, mechanical properties and fracture mechanism, Mater. Sci. Eng. A 663 (2016) 116–125.
[10] X.X. Zhang, A. Lutz, H. Andrä, M. Lahres, D. Sittig, E. Maawad, W.M. Gan, D. Knoop, An additively manufactured and direct-aged AlSi3.5Mg2.5 alloy with superior strength and ductility: micromechanical mechanisms, Int. J. Plast. 146 (2021) 103083.
[11] G. Ribarik, T. Ungar, J. Gubicza, MWP-fit: a program for multiple whole-profile fitting of diffraction peak profiles by ab initio theoretical functions, J. Appl. Crystallogr. 34 (2001) 669–676.
[12] G. Ribarik, J. Gubicza, T. Ungar, Correlation between strength and microstructure of ball-milled Al-Mg alloys determined by X-ray diffraction, Mater. Sci. Eng. A 387 (2004) 343–347.
[13] Y. Estrin, H. Mecking, A unified phenomenological description of work-hardening and creep based on one-parameter models, Acta Metall. 32 (1984) 57–70.

[14] G. Sainath, B.K. Choudhary, J. Christopher, E.I. Samuel, M.D. Mathew, Applicability of Voce equation for tensile flow and work hardening behaviour of P92 ferritic steel, Int. J. Press. Vessels Pip. 132 (2015) 1–9.
[15] X.X. Zhang, D. Knoop, H. Andrä, S. Harjo, T. Kawasaki, A. Lutz, M. Lahres, Multiscale constitutive modeling of additively manufactured Al-Si-Mg alloys based on measured phase stresses and dislocation density, Int. J. Plast. 140 (2021) 102972.
[16] X.X. Zhang, H. Andrä, S. Harjo, W. Gong, T. Kawasaki, A. Lutz, M. Lahres, Quantifying internal strains, stresses, and dislocation density in additively manufactured AlSi10Mg during loading-unloading-reloading deformation, Mater. Des. 198 (2021) 109339.
[17] X.X. Zhang, A. Lutz, H. Andrä, M. Lahres, W.M. Gan, E. Maawad, C. Emmelmann, Evolution of microscopic strains, stresses, and dislocation density during in-situ tensile loading of additively manufactured AlSi10Mg alloy, Int. J. Plast. 139 (2021) 102946.
[18] S. Harjo, T. Ito, K. Aizawa, H. Arima, J. Abe, A. Moriai, T. Iwahashi, T. Kamiyama, Current status of engineering materials diffractometer at J-PARC, Mater. Sci. Forum 681 (2011) 443–448.
[19] MAUD: Materials Analysis Using Diffraction, ⟨http://maud.radiographema.com/⟩ (Accessed on June 01, 2019).
[20] R. Oishi, M. Yonemura, Y. Nishimaki, S. Torii, A. Hoshikawa, T. Ishigaki, T. Morishima, K. Mori, T. Kamiyama, Rietveld analysis software for J-PARC, Nucl. Instrum. Methods Phys. Res. A 600 (2009) 94–96.
[21] T. Liu, M.D. Vaudin, J.R. Bunn, T. Ungar, L.N. Brewer, Quantifying dislocation density in Al-Cu coatings produced by cold spray deposition, Acta Mater. 193 (2020) 115–124.
[22] S.H. He, B.B. He, K.Y. Zhu, M.X. Huang, On the correlation among dislocation density, lath thickness and yield stress of bainite, Acta Mater. 135 (2017) 382–389.
[23] S.H. He, B.B. He, K.Y. Zhu, M.X. Huang, Evolution of dislocation density in bainitic steel: modeling and experiments, Acta Mater. 149 (2018) 46–56.
[24] M.A. Vicente Alvarez, J.R. Santisteban, P. Vizcaíno, G. Ribárik, T. Ungar, Quantification of dislocations densities in zirconium hydride by X-ray line profile analysis, Acta Mater. 117 (2016) 1–12.
[25] I.S. Yasnikov, Y. Estrin, A. Vinogradov, What governs ductility of ultrafine-grained metals? A microstructure based approach to necking instability, Acta Mater. 141 (2017) 18–28.
[26] E. Orowan, Problems of plastic gliding, Proc. Phys. Soc. 52 (1940) 8–22.
[27] X. Wu, N. Tao, Y. Hong, B. Xu, J. Lu, K. Lu, Microstructure and evolution of mechanically-induced ultrafine grain in surface layer of AL-alloy subjected to USSP, Acta Mater. 50 (2002) 2075–2084.
[28] Z.Y. Liang, X. Wang, W. Huang, M.X. Huang, Strain rate sensitivity and evolution of dislocations and twins in a twinning-induced plasticity steel, Acta Mater. 88 (2015) 170–179.
[29] P. Zhou, Z.Y. Liang, R.D. Liu, M.X. Huang, Evolution of dislocations and twins in a strong and ductile nanotwinned steel, Acta Mater. 111 (2016) 96–107.
[30] S. Harjo, T. Kawasaki, Y. Tomota, W. Gong, K. Aizawa, G. Tichy, Z.M. Shi, T. Ungar, Work hardening, dislocation structure, and load partitioning in lath martensite determined by in situ neutron diffraction line profile analysis, Metall. Mater. Trans. A 48a (2017) 4080–4092.
[31] A. Paknia, A. Pramanik, A.R. Dixit, S. Chattopadhyaya, Effect of size, content and shape of reinforcements on the behavior of Metal Matrix Composites (MMCs) under tension, J. Mater. Eng. Perform. 25 (2016) 4444–4459.
[32] J.F. Zhang, X.X. Zhang, Q.Z. Wang, B.L. Xiao, Z.Y. Ma, Simulation of anisotropic load transfer and stress distribution in SiCp/Al composites subjected to tensile loading, Mech. Mater. 122 (2018) 96–103.
[33] X. Gao, X.X. Zhang, L. Geng, Strengthening and fracture behaviors in SiCp/Al composites with network particle distribution architecture, Mater. Sci. Eng. A 740 (2019) 353–362.
[34] J.F. Zhang, H. Andrä, X.X. Zhang, Q.Z. Wang, B.L. Xiao, Z.Y. Ma, An enhanced finite element model considering multi strengthening and damage mechanisms in particle reinforced metal matrix composites, Compos. Struct. 226 (2019) 111281.
[35] J.F. Zhang, X.X. Zhang, Q.Z. Wang, B.L. Xiao, Z.Y. Ma, Simulations of deformation and damage processes of SiCp/Al composites during tension, J. Mater. Sci. Technol. 34 (2018) 627–634.
[36] J.C. Shao, B.L. Xiao, Q.Z. Wang, Z.Y. Ma, K. Yang, An enhanced FEM model for particle size dependent flow strengthening and interface damage in particle reinforced metal matrix composites, Compos. Sci. Technol. 71 (2011) 39–45.
[37] X.X. Zhang, H. Andrä, Crystal plasticity simulation of the macroscale and microscale stress–strain relations of additively manufactured AlSi10Mg alloy, Comp. Mater. Sci. 200 (2021) 110832.
[38] P.J. Withers, W.M. Stobbs, O.B. Pedersen, The application of the Eshelby Method of internal-stress determination to short fiber metal matrix composites, Acta Metall. 37 (1989) 3061–3084.
[39] G.I. Taylor, The mechanism of plastic deformation of crystals. Part I.—theoretical, Proc. R. Soc. Lon. Ser. A 145 (1934) 362–387.
[40] B. Clausen, T. Lorentzen, T. Leffers, Self-consistent modelling of the plastic deformation of FCC polycrystals and its implications for diffraction measurements of internal stresses, Acta Mater. 46 (1998) 3087–3098.
[41] Z.Y. Zhong, H.G. Brokmeier, W.M. Gan, E. Maawad, B. Schwebke, N. Schell, Dislocation density evolution of AA 7020-T6 investigated by in-situ synchrotron diffraction under tensile load, Mater. Charact. 108 (2015) 124–131.
[42] U.F. Kocks, Laws for work-hardening and low-temperature creep, J. Eng. Mater. Technol. Trans. ASME 98 (1976) 76–85.
[43] J.D. Teixeira, L. Bourgeois, C.W. Sinclair, C.R. Hutchinson, The effect of shear-resistant, plate-shaped precipitates on the work hardening of Al alloys: towards a prediction of the strength-elongation correlation, Acta Mater. 57 (2009) 6075–6089.
[44] C.S. Kaira, C. Kantzos, J.J. Williams, V. De Andrade, F. De Carlo, N. Chawla, Microstructural evolution and deformation behavior of Al-Cu alloys: a Transmission X-ray Microscopy (TXM) and micropillar compression study, Acta Mater. 144 (2018) 419–431.
[45] A. Pineau, A.A. Benzerga, T. Pardoen, Failure of metals I: brittle and ductile fracture, Acta Mater. 107 (2016) 424–483.
[46] R.L. Ma, C.Q. Peng, Z.Y. Cai, R.C. Wang, Z.H. Zhou, X.G. Li, X.Y. Cao, Manipulating the microstructure and tensile properties of selective laser melted Al-Mg-Sc-Zr alloy through heat treatment, J. Alloy. Compd. 831 (2020) 154773.
[47] J. Suryawanshi, K.G. Prashanth, S. Scudino, J. Eckert, O. Prakash, U. Ramamurty, Simultaneous enhancements of strength and toughness in an Al-12Si alloy synthesized using selective laser melting, Acta Mater. 115 (2016) 285–294.
[48] X.P. Li, X.J. Wang, M. Saunders, A. Suvorova, L.C. Zhang, Y.J. Liu, M.H. Fang, Z.H. Huang, T.B. Sercombe, A selective laser melting and solution heat treatment refined Al-12Si alloy with a controllable ultrafine eutectic microstructure and 25% tensile ductility, Acta Mater. 95 (2015) 74–82.
[49] R. Pokharel, A. Patra, D.W. Brown, B. Clausen, S.C. Vogel, G.T. Gray, An analysis of phase stresses in additively manufactured 304L stainless steel using neutron diffraction measurements and crystal plasticity finite element simulations, Int. J. Plast. 121 (2019) 201–217.
[50] S. Ghorbanpour, M.E. Alam, N.C. Ferreri, A. Kumar, B.A. McWilliams, S.C. Vogel, J. Bicknell, I.J. Beyerlein, M. Knezevic, Experimental characterization and crystal plasticity modeling of anisotropy, tension-compression asymmetry, and texture evolution of additively manufactured Inconel 718 at room and elevated temperatures, Int. J. Plast. 125 (2020) 63–79.
[51] S. Ghorbanpour, M. Zecevic, A. Kumar, M. Jahedi, J. Bicknell, L. Jorgensen, I.J. Beyerlein, M. Knezevic, A crystal plasticity model incorporating the effects of precipitates in superalloys: application to tensile, compressive, and cyclic deformation of Inconel 718, Int. J. Plast. 99 (2017) 162–185.